Altered interplay between endoplasmic reticulum and mitochondria in Charcot–Marie–Tooth type 2A neuropathy

Nathalie Bernard-Marissal[a,b,1], Gerben van Hameren[c], Manisha Juneja[d,e], Christophe Pellegrino[f], Lauri Louhivuori[g], Luca Bartesaghi[h,i], Cylia Rochat[a], Omar El Mansour[a], Jean-Jacques Médard[h,i], Marie Croisier[j], Catherine Maclachlan[j], Olivier Poirot[k], Per Uhlén[g], Vincent Timmerman[d,e], Nicolas Tricaud[c], Bernard L. Schneider[a,1,2], and Roman Chrast[h,i,1,2]

[a]Brain Mind Institute, École Polytechnique Fédérale de Lausanne, 1015 Lausanne, Switzerland; [b]Marseille Medical Genetics, INSERM, Aix-Marseille Univ, 13385 Marseille, France; [c]INSERM U1051, Institut des Neurosciences de Montpellier, Université de Montpellier, 34295 Montpellier, France; [d]Peripheral Neuropathy Research Group, Department of Biomedical Sciences, University of Antwerp, 2610 Antwerp, Belgium; [e]Institute Born Bunge, 2610 Antwerp, Belgium; [f]Institut de Neurobiologie de la Méditerranée, INSERM, Aix-Marseille Univ, 13009 Marseille, France; [g]Department of Medical Biochemistry and Biophysics, Karolinska Institutet, 17177 Stockholm, Sweden; [h]Department of Neuroscience, Karolinska Institutet, 17177 Stockholm, Sweden; [i]Department of Clinical Neuroscience, Karolinska Institutet, 17177 Stockholm, Sweden; [j]Centre of Interdisciplinary Electron Microscopy, École Polytechnique Fédérale de Lausanne, 1015 Lausanne, Switzerland; and [k]Department of Medical Genetics, University of Lausanne, 1005 Lausanne, Switzerland

Edited by Stephen T. Warren, Emory University School of Medicine, Atlanta, GA, and approved December 14, 2018 (received for review June 26, 2018)

Mutations in the *MFN2* gene encoding Mitofusin 2 lead to the development of Charcot–Marie–Tooth type 2A (CMT2A), a dominant axonal form of peripheral neuropathy. Mitofusin 2 is localized at both the outer membrane of mitochondria and the endoplasmic reticulum and is particularly enriched at specialized contact regions known as mitochondria-associated membranes (MAM). We observed that expression of $MFN2^{R94Q}$ induces distal axonal degeneration in the absence of overt neuronal death. The presence of mutant protein leads to reduction in endoplasmic reticulum and mitochondria contacts in CMT2A patient-derived fibroblasts, in primary neurons and in vivo, in motoneurons of a mouse model of CMT2A. These changes are concomitant with endoplasmic reticulum stress, calcium handling defects, and changes in the geometry and axonal transport of mitochondria. Importantly, pharmacological treatments reinforcing endoplasmic reticulum–mitochondria cross-talk, or reducing endoplasmic reticulum stress, restore the mitochondria morphology and prevent axonal degeneration. These results highlight defects in MAM as a cellular mechanism contributing to CMT2A pathology mediated by mutated MFN2.

motoneurons | endoplasmic reticulum | mitochondria | CMT2A | neuropathy

Charcot–Marie–Tooth (CMT) disease, also known as hereditary motor and sensory peripheral neuropathy, represents a clinically heterogeneous group of inherited neurological disorders with a prevalence of 1 in 2,500 (1, 2). These diseases result from defects in axons or in myelin or in both. Among the axonal forms of CMT, around 10 to 20% are linked to mutations in the *MFN2* gene, encoding Mitofusin 2, and are referred to as CMT2A (3–5). The symptoms of CMT2A are mainly characterized by progressive distal muscle weakness and atrophy, foot deformities, areflexia, and sensory loss (6). However, the age of disease onset and the severity of symptoms are highly variable among CMT2A patients (6).

MFN2 is a dynamin-like GTPase protein originally identified at the outer membrane of mitochondria, where it regulates mitochondrial fusion (7). Characterization of in vitro and in vivo models of the disease based on the expression of mutated MFN2 has led to substantial insights into the CMT2A pathophysiology (8–12). Multiple mouse models have been developed for CMT2A (8, 13–15); however, a transgenic line overexpressing $MFN2^{R94Q}$ specifically in neurons (mitoCharc mice or *CMT2A Tg*) most closely mimics the late-onset CMT2A pathology (8). *CMT2A Tg* mice develop locomotor dysfunction from the age of 5 mo on, a pathologic effect associated at a late stage of the disease with the accumulation of mitochondria in small-caliber axons (8). However, the long-term progression of the disease and the mechanisms underlying motor and/or sensory dysfunction have not been fully characterized in this model. In vitro, primary sensory and motor neurons overexpressing mutated *MFN2*, or motoneurons differentiated from CMT2A iPS cells, both display mild defects in mitochondrial transport as well as mitochondrial fragmentation (10–12, 14–16). In sensory neurons expressing $MFN2^{R94Q}$, overexpression of the homologous mitochondrial protein MFN1 partially restores mitochondrial fusion and rescues mitochondrial transport and axonal degeneration (10), suggesting the existence of additional mechanisms underlying the $MFN2^{R94Q}$-related pathophysiology.

Interestingly, a fraction of MFN2 is also located at the endoplasmic reticulum (ER) membrane, in particular at specialized sites of contacts with mitochondria called mitochondria-associated membranes (MAM) (17). The MAM control several cellular

Significance

Interactions between mitochondria and the endoplasmic reticulum (ER) at the level of mitochondria-associated membranes (MAM) constitute a key signaling hub, emerging as a shared target altered in multiple neurodegenerative diseases. We use both in vivo and in vitro models of Charcot–Marie–Tooth type 2A, an axonal form of neuropathy, to demonstrate that the presence of mutated Mitofusin 2 leads to altered MAM. In neurons, these modifications occur concomitantly with activation of ER stress response, dysregulated calcium handling, and alterations in mitochondrial morphology and transport, collectively contributing to axonopathy. Importantly, the reported results indicate that the pathological consequences of mutated Mitofusin 2 may be targeted with drugs reinforcing the ER–mitochondria cross-talk and/or reducing ER stress.

Author contributions: N.B.-M., O.P., P.U., V.T., N.T., B.L.S., and R.C. designed research; N.B.-M., G.v.H., M.J., C.P., L.L., L.B., C.R., O.E.M., J.-J.M., M.C., C.M., and O.P. performed research; N.B.-M., G.v.H., M.J., C.P., L.L., L.B., O.P., P.U., V.T., N.T., B.L.S., and R.C. analyzed data; and N.B.-M., B.L.S., and R.C. wrote the paper.

The authors declare no conflict of interest.

This article is a PNAS Direct Submission.

[1]To whom correspondence may be addressed. Email: nathalie.bernard.1@univ-amu.fr, bernard.schneider@epfl.ch, or roman.chrast@ki.se.

[2]B.L.S. and R.C. contributed equally to this work.

This article contains supporting information online at www.pnas.org/lookup/suppl/doi:10.1073/pnas.1810932116/-/DCSupplemental.

processes such as lipid metabolism, calcium homeostasis, mitochondrial dynamics, and autophagy/mitophagy (18, 19). Several studies have highlighted the role of MAM in neuronal function, with important implications in various neurodegenerative disorders (20–25). MFN2 has been proposed to regulate either positively or negatively the association between the two organelles (17, 26–28). However, it is unknown how CMT2A-associated MFN2 mutations affect MAM functioning and what the potential consequences for CMT2A pathology are. In addition to MFN2, mutations in other mitochondrial proteins including GDAP1, OPA1, DNM1L, ATAD3A, and SLC25A46 affect mitochondrial biology and lead to neurological diseases (29, 30). Similarly, mutations in proteins affecting shape and function of ER including FAM134B, ATL1, ATL3, and BSCL2 are linked to disturbed neuronal function (2). These studies indicate the importance of both mitochondrial and ER physiology and interorganelle communication in the field of neuropathy.

In the present study, we characterized in detail the neuropathy phenotype caused by expression of $MFN2^{R94Q}$ in both in vitro and in vivo CMT2A disease models. Our data show that overexpression of $MFN2^{R94Q}$ affects locomotion and gait in *CMT2A Tg* mice and causes the loss of neuromuscular junctions at a late stage of the disease. In primary neurons, $MFN2^{R94Q}$ induces axonal degeneration. At the cellular level, $MFN2^{R94Q}$ expression leads to the loss of MAM, ER stress, intracellular calcium handling defects, and impaired mitochondrial dynamics. Importantly, we observe that pharmacological treatments to reinforce MAM function or block ER stress can rescue some of the axonal and mitochondrial phenotypes caused by $MFN2^{R94Q}$.

Results

***CMT2A Tg* Mice Display Locomotor and Gait Abnormalities Associated with Slow-Twitch Muscle Denervation.** Previous studies showed that heterozygous (line hMFN2R94QL51, MitoCharc1) and homozygous (line hMFN2R94QL87, MitoCharc2) *CMT2A Tg* mice develop locomotion impairments in the rotarod test, starting from the age of ∼6 mo (8). As CMT2A patients display symptoms that worsen with age (31), we sought to assess the progression of both motor and sensory dysfunctions in *CMT2A Tg* mice. To mimic the dominant inheritance of CMT2A we used heterozygous *B6;D2-Tg* $^{(Eno2\text{-}MFN2*R94Q)/-}$ mice [originally named hMFN2R94QL51, MitoCharc1 (8)], hereafter referred as *CMT2A Tg* mice. We performed a battery of behavioral tests at early and late time points (6 and 12 mo of age). Mouse locomotor function was evaluated using the rotarod and CatWalk gait analysis, whereas their sensory sensitivity to a mechanical stimulus was evaluated using the Von Frey test which is based on evaluation of the mechanical force able to elicit a paw withdrawal response (32). We did not observe any significant effect in sensory function (Fig. 1*A*). However, the performance on the rotarod was significantly affected in *CMT2A Tg* animals compared with WT littermates at both 6 and 12 mo of age (Fig. 1*B*). In the group of *CMT2A Tg* mice, the latency to fall from the rotarod did not significantly decrease between 6 and 12 mo (Fig. 1*B* and *SI Appendix*, Fig. S1*A*). Furthermore, analysis of the rotarod results according to mouse sex showed that the motor performance was significantly decreased in male but not in female *CMT2A Tg* mice (*SI Appendix*, Fig. S1*A*).

The CatWalk test revealed that several gait parameters were significantly changed at both 6 and 12 mo in *CMT2A Tg* mice compared with WT mice. These parameters were classified as indicators of the pressure exerted by each paw, the area of the floor contacted by each paw, gait/posture, and coordination (*SI Appendix*, Table S1). Intensity variables reflecting paw pressure during contact with the glass walkway floor were reported to be affected by peripheral nerve injury (33). Here, forepaw intensity values were significantly decreased in *CMT2A Tg* animals at both time points (*SI Appendix*, Table S1). Print size of the right

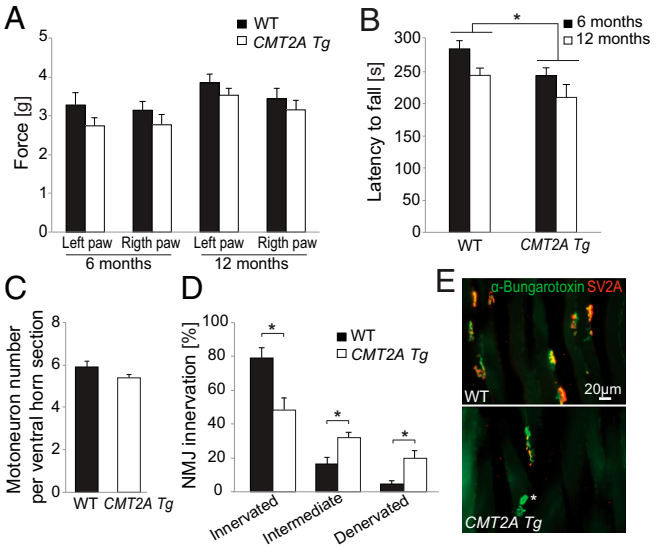

Fig. 1. *CMT2A Tg* mice show locomotor defects and muscle denervation but no detectable motoneuronal death. (*A*) Evaluation of sensory function with the von Frey test at the age of 6 and 12 mo (WT: $n = 11$ and *CMT2A Tg*: $n = 12$). Statistical analysis: two-way repeated-measures ANOVA (group × time) with Newman–Keuls post hoc test. (*B*) Evaluation of motor function with rotarod test at the age of 6 and 12 mo (WT: $n = 11$ and *CMT2A Tg*: $n = 12$). Statistical analysis: two-way repeated-measures ANOVA (group × time, significant group effect) with Newman–Keuls post hoc test. (*C*) Number of motoneurons in lumbar spinal cord of 12-mo-old animals ($n = 4$ for both WT and *CMT2A Tg*). Statistical analysis: two-tailed unpaired Student's *t* test. (*D*) Level of innervation of soleus muscle evaluated based on the colocalization of the nerve terminal marker SV2A and acetylcholine receptor marker α-bungarotoxin in 12-mo-old WT ($n = 5$) and *CMT2A Tg* ($n = 7$) mice. Statistical analysis: two-tailed unpaired Student's *t* test. (*E*) Representative photomicrographs of NMJ in WT and *CMT2A Tg* soleus muscle, stained with anti-SV2A antibodies and α-bungarotoxin. Note the presence of unoccupied NMJ positive for α-bungarotoxin only (indicated by an asterisk) in the *CMT2A Tg* mice. $*P < 0.05$.

forepaw was also reduced in 6-mo-old *CMT2A Tg* mice, suggesting a misplacement of the paw (*SI Appendix*, Table S1). Dynamic CatWalk variables that evaluate gait/posture as well as coordination were also affected in *CMT2A Tg* mice. At the age of 6 mo, right forepaw terminal dual stance and left forepaw duty cycle mean were increased, whereas two other variables (left hindpaw stand mean and "support three") also indicating gait impairment were significantly changed in 12-mo-old *CMT2A Tg* animals (*SI Appendix*, Table S1). These observations indicate that *CMT2A Tg* mice maintain some of their paws longer on the glass plate. Finally, the right forepaw and right hindpaw interpaw coordination reflected by the phase dispersions and couplings parameters were altered in *CMT2A Tg* mice only at 12 mo (*SI Appendix*, Table S1).

To assess whether these locomotor defects were linked to muscle weakness, we monitored muscle strength using the grid test (34, 35). No decrease in muscle strength score was observed in *CMT2A Tg* mice compared with WT at either 6 (WT: 2,308 ± 96.2 and *CMT2A Tg*: 2,328 ± 144.8) or 12 mo (WT: 1,886 ± 107.7 and *CMT2A Tg*: 1,852 ± 155.2).

As defects in locomotion can reflect subtler neuromuscular dysfunctions, we evaluated motoneuron survival and neuromuscular junction (NMJ) innervation. We did not observe any loss of motoneurons in *CMT2A Tg* spinal cord at 12 mo (Fig. 1*C*). Similarly, there was no significant loss of proximal motor axons in the ventral roots or sensory neurons in the dorsal root (*SI Appendix*, Fig. S1 *B* and *C*). However, we observed a significant decrease in the proportion of fully innervated NMJ at the age of

12 mo in the slow-twitch soleus muscle of *CMT2A Tg* mice (innervated NMJ WT: 79 ± 5.8%, *CMT2A Tg*: 48.2 ± 7%) (Fig. 1 *D* and *E*). Remarkably, at the same age, NMJ occupancy was not significantly reduced in the fast-twitch tibialis muscle (*SI Appendix*, Fig. S1*D*), and electrophysiological recording of the compound muscle action potential (CMAP) did not show any significant decrease in amplitude in *CMT2A Tg* mice (*SI Appendix*, Fig. S1*E*). These results were consistent with preserved muscle strength (dependent on gastrocnemius and tibialis muscles) measured with the grid test in the *CMT2A Tg* mice until 12 mo. Moreover, NMJ innervation was not affected at 6 mo in the soleus muscle (*SI Appendix*, Fig. S1*F*), suggesting that additional mechanisms may underlie the behavioral dysfunctions already observed at this age, and possibly involve other distal muscle groups.

MFN2^{R94Q} Overexpression Reduces Neurite Length of Primary Motoneurons. To characterize the mechanisms underlying neuronal dysfunction in CMT2A, we used primary embryonic cultures of either motor or sensory neurons, the two neuronal populations that are typically affected by the disease. To evaluate the effects of mutated CMT2A, we overexpressed either the WT (*MFN2^{WT}*) or R94Q mutated form of MFN2 (*MFN2^{R94Q}*) using AAV6 vectors (*SI Appendix*, Fig. S2*A*). In accordance with our in vivo data, the overexpression of either *MFN2^{WT}* or *MFN2^{R94Q}* did not reduce the survival of motor or sensory neurons at 4, 6, or 8 d postinfection (dpi) (Fig. 2 *A* and *B*). However, the overexpression of *MFN2^{R94Q}* led to a significant reduction of neuritic length at 6 dpi. This effect was evident in motoneurons (noninfected: 1,982.6 ± 220.9, *MFN2^{WT}*: 2,056.8 ± 175.7 μm, *MFN2^{R94Q}*: 1,419.5 ± 110.5 μm) but not in sensory neurons (*MFN2^{WT}*: 3,810 ± 648 μm, *MFN2^{R94Q}*: 3,547 ± 897 μm) (Fig. 2 *C* and *D*). Moreover, in both motor and sensory neurons expressing *MFN2^{R94Q}* we observed the presence of axonal swellings and spheroids, as revealed by peripherin staining (Fig. 2*D*).

MFN2^{R94Q} Impairs ER–Mitochondria Tethering both in Vitro and in Vivo. MFN2 has been shown to regulate either positively or negatively ER–mitochondria connections (17, 26–28). We therefore quantified ER–mitochondria contacts in neurons overexpressing either WT or mutated MFN2. We used an in vitro proximity ligation assay (PLA) based on the interaction of the mitochondrial VDAC1 protein and the ER protein IP3R, as previously described (22) (*SI Appendix*, Fig. S2*B*). The number of dots reflecting ER–mitochondria contacts was significantly decreased in both motor and sensory neurons overexpressing MFN2^{R94Q}, compared with both noninfected neurons and neurons overexpressing MFN2^{WT} (Fig. 3 *A* and *B*). To determine if similar defects can be observed in CMT2A pathology, PLA was also performed in CMT2A patient-derived fibroblasts. Compared with control fibroblast cell lines, we again observed a significant decrease in the number of ER–mitochondria contacts (Fig. 3 *C* and *D*). As overexpression of MFN2 in cell lines can induce changes in various mitochondrial parameters (36), we investigated if the reduced number of contacts observed in both CMT2A neurons and fibroblasts as well as neuronal neurite shortening could be primarily caused by morphological alterations of mitochondria. Based on localization of myc-MFN2 and myc-MFN1, we did not observe any obvious clustering of mitochondria in neurons overexpressing MFN2^{WT} or MFN2^{R94Q} (*SI Appendix*, Fig. S2 *A* and *E*). Furthermore, we evaluated the impact of overexpression of MFN1, which has been reported to effectively complement this CMT2A mutant protein for mitochondrial fusion (37). Motoneuron cultures transduced with an AAV6 vector expressing either GFP or MFN2^{R94Q} were cotransduced with an AAV6-MFN1 vector (using a total vector dose similar to the previous experiment). MFN1 coexpression did not significantly change the number of ER–mitochondria contacts, which was still

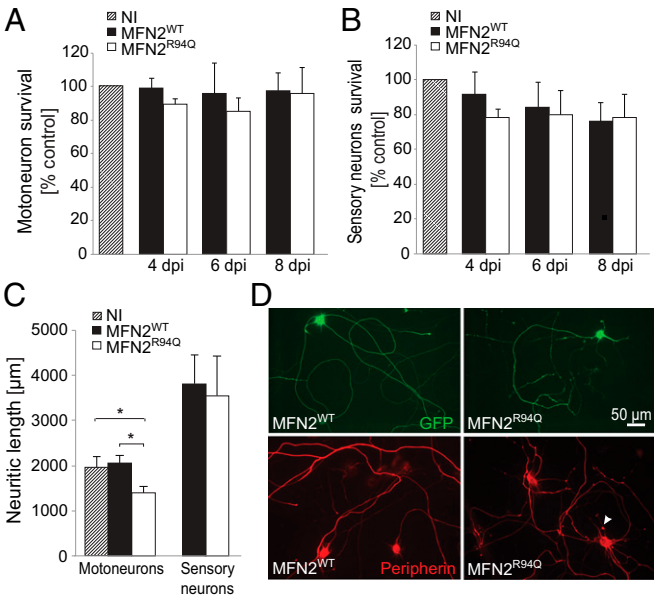

Fig. 2. Overexpressing MFN2^{R94Q} induces neurite degeneration in the absence of neuronal death. (*A* and *B*) Motor and sensory neurons were infected for 4, 6, and 8 dpi with AAV6-hsyn-hMFN2^{WT} or AAV6-hsyn-hMFN2^{R94Q}. Survival of motor and sensory neurons was evaluated following SMI32 and NF-200 staining. Noninfected (NI) neuron cultures were used as a control to evaluate the effect of MFN2 overexpression. Data are expressed as mean percentage ± SEM compared with the NI control cultures (n = 3 independent neuronal cultures). Statistical analysis: two-way ANOVA (group × time), with Tukey's post hoc test. (*C*) Neuritic length was quantified at 6 dpi in motor and sensory neurons infected with AAV6-hsyn-hMFN2^{WT} or AAV6-hsyn-hMFN2^{R94Q}. Neurons were cotransduced with AAV6-CMV-GFP to label neurites. Values are expressed as mean (micrometers) ± SEM from six (motoneurons) and three (sensory neurons) independent cultures. Statistical analysis: two-way ANOVA (group × time), with Tukey's post hoc test. (*D*, *Upper*) GFP-labeled neurites in motoneurons expressing either MFN2^{WT} or MFN2^{R94Q}. (*D*, *Lower*) Peripherin staining in the same conditions. Arrowhead indicates a peripherin-positive axonal swelling. *P < 0.05.

decreased in neurons overexpressing MFN2^{R94Q} (*SI Appendix*, Fig. S2*C*). Furthermore, we did not observe any significant effect of MFN1 on neurite shortening in MFN2^{R94Q}-expressing motoneurons (*SI Appendix*, Fig. S2*D*). Similar to neurons, MFN1 expression in patient-derived fibroblasts also did not significantly change the reduced number of ER–mitochondria contacts (*SI Appendix*, Fig. S2 *E* and *F*). These data suggest that the MAM and neuritic defects observed in CMT2A context cannot be rescued by MFN1 overexpression.

Next, we further evaluated by electron microscopy the contacts between mitochondria and ER, in the motoneuron soma in the lumbar spinal cord of 12-mo-old WT and *CMT2A Tg* mice. In WT mice, 37.8 ± 2.1% of the mitochondria made at least one contact with the ER, whereas this proportion was significantly decreased in *CMT2A Tg* motoneurons (31.3 ± 2.1%) (Fig. 3 *E* and *G*). Furthermore, the length of these contacts was significantly decreased in *CMT2A Tg* motoneurons, representing only 6.0 ± 0.3% of mitochondrial perimeter, as compared 9.6 ± 0.4% in their WT counterparts (Fig. 3 *F* and *G*). We did not notice any significant change in the level of expression of SIGMAR1 or VAPB, two constituents of MAM, in the spinal cord of CMT2A mice, supporting a specific role of mutated MFN2 in the observed MAM defects (*SI Appendix*, Fig. S2 *G* and *H*). To determine whether the altered contacts between ER and mitochondria played a functional role in neurite shortening following MFN2^{R94Q} expression, we treated motoneurons with Pre-084 a selective agonist of SIGMAR1, a chaperone protein located at the

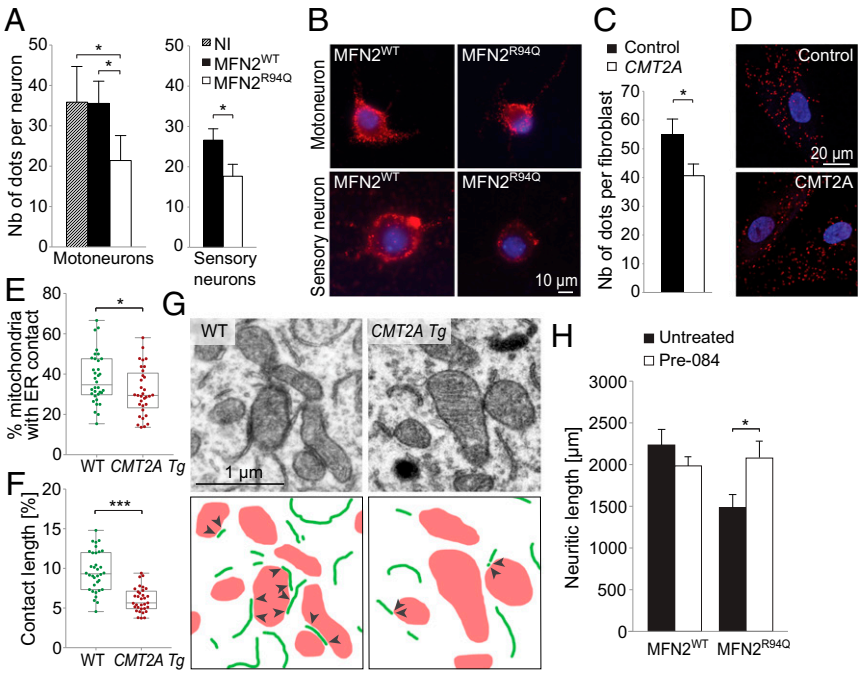

Fig. 3. MFN2^{R94Q} affects neuronal ER–mitochondria contacts in vitro and in vivo. (*A*) Quantification of ER–mitochondria contacts using PLA at 6 dpi in motor ($n = 5$ independent cultures) and sensory neurons ($n = 3$), infected with AAV6-hsyn-hMFN2^{WT} or AAV6-hsyn-hMFN2^{R94Q} ($n = 6$ independent cultures). Data are expressed as the mean number of contacts ± SEM per neuron detected by a PLA. Statistical analysis: repeated measures one-way ANOVA with Tukey's post hoc test (motoneurons) and two-tailed paired Student's *t* test (sensory neurons). NI, noninfected motoneurons. (*B*) Photomicrographs of PLA between the ER protein IP3R and the mitochondrial protein VDAC1 in motor and sensory neurons. Red dots indicate ER–mitochondria proximity. Nuclei are stained with DAPI. (*C*) Quantification of ER–mitochondria contacts using PLA in fibroblasts from control and CMT2A-R94Q individuals ($n = 39$ and $n = 40$ cells, respectively, from two independent cell lines for each condition). Data are expressed as the mean number of contacts ± SEM per cell. Statistical analysis: two-tailed unpaired Student's *t* test. (*D*) Photomicrographs of control and *CMT2A* human fibroblasts. Intracellular red dots indicate the presence of ER–mitochondria proximity revealed by the PLA. Nuclei are stained with DAPI. (*E*) Electron microscopy quantification of the percentage of mitochondria with ER contact in motoneuron soma in the lumbar spinal cord of 12-mo-old WT ($n = 34$ motoneurons from three mice) and *CMT2A Tg* mice ($n = 33$ motoneurons from three mice). Statistical analysis: two-tailed unpaired Student's *t* test. (*F*) Analysis of the length of the mitochondria–ER contacts, expressed as the percentage of the mitochondrial perimeter ($n = 34$ motoneurons from three WT mice and $n = 33$ motoneurons from three *CMT2A Tg* mice). Statistical analysis: two-tailed unpaired Student's *t* test. (*G*) Electron microscopy pictures illustrating ER–mitochondria contacts in motoneuron soma of WT and *CMT2A Tg* mice. ER segments are delineated in green and mitochondria are shown in red. Arrowheads indicate the mitochondria–ER contacts. (*H*) Neuritic length quantified at 6 dpi in motoneurons overexpressing either MFN2^{WT} or MFN2^{R94Q}. Motoneurons treated with a SIGMAR1 agonist (Pre-084, 50 nM) are compared with the untreated condition. Note the significant rescue of neuritic length in MFN2^{R94Q} motoneurons treated with Pre-084. Mean values are obtained from four independent cultures. Statistical analysis: two-way ANOVA (group × treatment) with Sidak post hoc test. $*P < 0.05$, $***P < 0.001$.

MAM which controls calcium transfer from the ER toward mitochondria (22). Remarkably, exposure of primary motoneurons to Pre-084 almost completely prevented neurite degeneration induced by MFN2^{R94Q}, as shown by significant increase in neuritic length compared with untreated neurons (MFN2^{R94Q}: 1,479 ± 162 µm, MFN2^{R94Q} + Pre-084: 2,087.5 ± 187.9 µm) (Fig. 3*H*).

Expression of MFN2^{R94Q} Leads to Unfolded Protein Response Activation and Intracellular Calcium Defects. MAM defects have been previously linked to ER malfunction leading to an unfolded protein response (UPR) and calcium homeostasis impairments (22, 38). We therefore analyzed the level of ER stress markers in vitro (phosphorylated eIF2A, P-eIF2α; the ER chaperone PDI). The levels of both P-eIF2α and PDI were significantly increased in motoneurons overexpressing mutated MFN2 relative to MFN2^{WT} (PDI MFN2^{R94Q}: +71.2 ± 21.0% compared with MFN2^{WT}; P-eIF2α MFN2^{R94Q}: +134 ± 53.4% compared with MFN2^{WT}) (Fig. 4 *A* and *B*). In sensory neurons, there was no significant effect of MFN2^{R94Q} on the level of both PDI and P-eIF2α (Fig. 4*A*).

To confirm these findings in vivo, we analyzed the level of P-eIF2α, PDI, and activating transcription factor 6 (ATF6) in lumbar motoneurons of 12-mo-old *CMT2A Tg* animals. Compared with WT littermates, we observed a significant increase in PDI expression similar to the changes seen in vitro (Fig. 4 *C* and *E*). Although there was a clear trend toward increased level of P-eIF2α, the difference did not reach statistical significance (Fig. 4*C*). We also analyzed the nuclear translocation of ATF6 as an additional early marker of ER stress in motoneurons of WT and *CMT2A Tg* mice. The proportion of motoneurons with a predominant nuclear vs. cytosolic ATF6 staining was significantly higher in the *CMT2A Tg* lumbar spinal cord (WT: 24 ± 3.2%, *CMT2A Tg*: 47.4 ± 5.2%) (Fig. 4 *D* and *E*).

Interestingly, exposure of primary motoneurons to the ER stress inhibitor salubrinal (22) almost completely prevented neurite degeneration induced by MFN2^{R94Q}, as shown by a significant increase in neuritic length compared with untreated neurons (MFN2^{R94Q}: 1,270.7 ± 77.8 µm, MFN2^{R94Q} + salubrinal: 1,685.5 ± 115.6 µm) (Fig. 4*F*). These results show that ER stress plays a functional role in neuronal degeneration following MFN2^{R94Q} expression.

We also monitored intracellular calcium variation in motor and sensory neurons using ratiometric Fura-Red AM calcium dye before, during, and after 25 mM KCl exposure, as previously described (39). In basal conditions, we did not detect any difference in the ratiometric fluorescence of the calcium indicator when comparing motoneurons overexpressing either MFN2^{WT} or MFN2^{R94Q}, indicating no difference in basal calcium loading

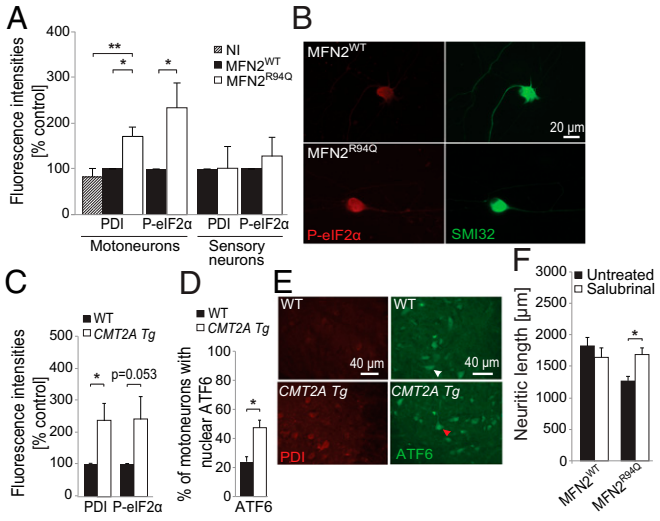

Fig. 4. MFN2^{R94Q} induces ER stress both in vitro and in vivo. (*A*) Immunoquantification of level of ER stress in motor and sensory neurons infected with AAV6-hsyn-hMFN2^{WT} or AAV6-hsyn-hMFN2^{R94Q} at 6 dpi (n = 5 and 3 independent cultures for motor and sensory neurons, respectively). Levels of PDI or P-eIF2α were normalized to the level of either the motoneuronal marker SMI32 or the sensory neuron marker NF-200. Data are expressed as percentage ±SEM relative to MFN2^{WT} condition. Statistical analysis: one-way ANOVA with Tukey's post hoc test. NI, noninfected motoneurons. (*B*) Representative stainings for P-eIF2α and SMI32 in motoneurons expressing MFN2^{WT} or MFN2^{R94Q}. (*C*) Immunoquantification of ER stress markers in motoneurons in the lumbar spinal cord of 12-mo-old WT (n = 6) and *CMT2A Tg* mice (n = 6). Levels of P-eIF2α and PDI were normalized to the neuronal marker NeuN. Data are expressed as percentage ± SEM relative to WT. Statistical analysis: two-tailed unpaired Student's t test. (*D*) The percentage of motoneurons with nuclear vs. cytoplasmic ATF6 was evaluated in the spinal cord of 12-mo-old WT (n = 6) and *CMT2A Tg* mice (n = 5). Statistical analysis: two-tailed unpaired Student's t test. (*E*) Representative photomicrographs of PDI (*Left*) and ATF6 staining (*Right*) in WT and *CMT2A Tg* spinal cord sections. Cytoplasmic and nuclear ATF6 staining is indicated by arrowheads. (*F*) Neuritic length quantified at 6 dpi in motoneurons overexpressing either MFN2^{WT} or MFN2^{R94Q}. Motoneurons were treated with salubrinal (5 μM). Values represent the mean of four independent cultures. Statistical analysis: two-way ANOVA (group × treatment) with Sidak post hoc test. *P < 0.05, **P < 0.01.

(Fig. 5 *A* and *B*). However, we found a lower amplitude in the KCl-evoked calcium rise in MFN2^{R94Q} motoneurons, compared with cells expressing MFN2^{WT} (Fig. 5*C*), while there was no difference in normalized half-time recovery (Fig. 5*D*). The data from sensory neurons (Fig. 5 *E–H*) also revealed changes in calcium homeostasis, showing alterations in the basal calcium loading (Fig. 5*F*), a lower amplitude in the KCl-evoked calcium rise in MFN2^{R94Q} (Fig. 5*G*), and an increase in time to return to basal calcium levels (Fig. 5*H*).

To further elucidate the possible perturbations in $[Ca^{2+}]_i$ homeostasis, we examined the global $[Ca^{2+}]_i$ dynamics in CMT2A patient-derived fibroblasts and control fibroblasts (Fig. 5*I*). To determine whether an impairment in ER handling of $[Ca^{2+}]_i$ was present, we examined the difference in ER Ca^{2+} discharge between control and patient cells by challenging the cells in Ca^{2+}-free conditions with thapsigargin (2 μM), a compound known to induce Ca^{2+} release from the ER by inhibiting Ca^{2+} sarco/endoplasmic reticulum Ca^{2+}-ATPase pumps. Remarkably, a significant drop in the $[Ca^{2+}]_i$ baseline steady state was observed between patient and control cells (0.18 ± 0.017 vs. 0.31 ± 0.021; Fig. 5 *J* and *K*) when extracellular Ca^{2+} was removed by EDTA chelation before the application of thapsigargin. Applying thapsigargin resulted in a significantly lower amplitude of the

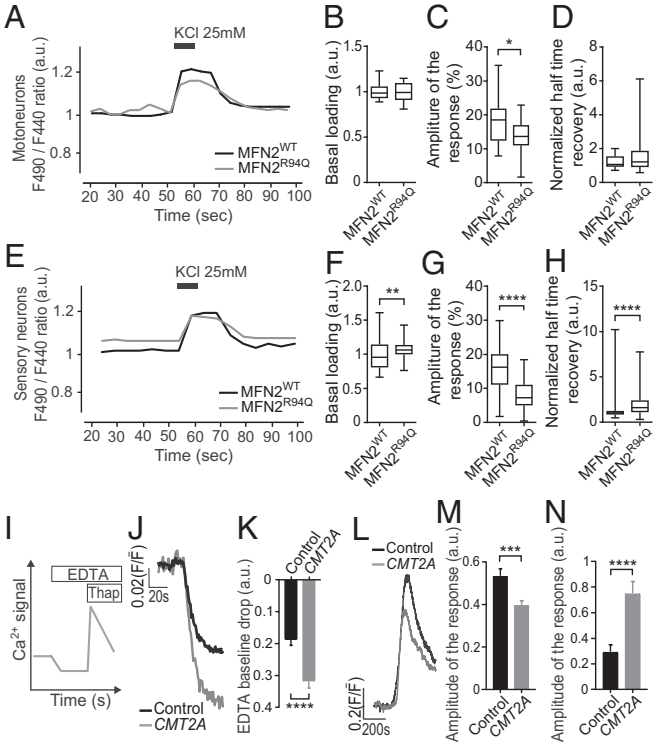

Fig. 5. MFN2^{R94Q} induces changes in calcium homeostasis both in vitro and in vivo. (*A–D*) Intracellular calcium measurements using Fura-Red ratiometric imaging (F490/F440) after KCl (25 mM) exposure of MFN2^{WT} (n = 16) and MFN2^{R94Q} (n = 25) motoneurons. (*A*) An example of obtained recordings. Basal loading was determined as the average of resting calcium concentration (F490/F440, represented as arbitrary units, a.u.) between 20 and 50 s of measurement. (*B*) Basal loading levels. (*C*) Amplitude of the maximal response obtained after 8-s exposure to KCl (25 mM), expressed as the percentage of variation relative to basal fluorescence determined in *B*. (*D*) Representation of normalized half-time recovery (50% return to basal level normalized by the amplitude of response). (*E–H*) Intracellular calcium measurements using Fura-Red ratiometric imaging (F490/F440) after 8-s KCl (25 mM) exposure of MFN2^{WT} (n = 105) and MFN2^{R94Q} (n = 81) sensory neurons. (*E*) An example of obtained recordings. Basal loading was determined as the average of resting calcium concentration (F490/F440, represented as arbitrary units, a.u.) between 20 and 50 s of measurement. (*F*) Basal loading levels. (*G*) Amplitude of the maximal response obtained after exposure to KCl (25 mM), expressed as the percentage of variation relative to basal fluorescence. (*H*) Representation of normalized half-time recovery (50% return to basal level normalized by the amplitude of response). (*I–M*) Intracellular calcium measurements in control and CMT2A patient-derived fibroblasts evaluated by Fluo-4 AM fluorescent microscopy. Calcium dynamics are expressed as the ratio of fluorescence intensity (F) divided by the mean fluorescence (F̄) averaged over the first 50 frames and represented as a.u. (controls, n = 100 and CMT2A, n = 102). (*I*) A schematic overview of the experimental setting for *J–M*. (*J*) Example of a recording obtained in a fibroblast exposed to extracellular EDTA. (*K*) Quantification of the drop in intracellular calcium determine as a difference between baseline value and the maximal drop in intracellular calcium induced by presence of extracellular EDTA. (*L*) Example of a recording obtained in a fibroblast exposed to thapsigargin. (*M*) Quantification of the change determined as a difference between baseline value and the maximal response in intracellular calcium induced by thapsigargin. Values represent the data from three independent cultures. (*N*) Quantification of the change determined as a difference between baseline value and the maximal response in intracellular calcium released from mitochondria following exposure to CCCP (2 μM). Values represent the data from three independent cultures. Controls, n = 82 and *CMT2A*, n = 34. Data are expressed as box-and-whisker plots or as mean ± SEM. Statistical analysis: two-tailed unpaired Student's t test. *P < 0.05, **P < 0.01, ***P < 0.001, and ****P < 0.0001.

$[Ca^{2+}]_i$ response in patient cells compared with controls (0.53 ± 0.033 vs. 0.39 ± 0.019; Fig. 5 *L* and *M*).

Mitochondria play a role in the uptake of Ca^{2+} from the cytosol, in particular in presence of high $[Ca^{2+}]_i$ levels. We used the protonophore CCCP (carbonyl cyanide m-chlorophenyl hydrazone), which collapses the mitochondrial membrane potential, to release Ca^{2+} from the mitochondria. As seen in Fig. 5*N* and *SI Appendix*, Fig. S3*A*, the level of Ca^{2+} discharged as a result of bath application of CCCP (2 μM) was significantly higher in CMT2A fibroblasts than in their respective controls, which indicates that mitochondria may accumulate abnormally high levels of Ca^{2+} in these cells.

Mitochondrial Transport and Clustering Are Altered in Axons Expressing $MFN2^{R94Q}$. Previous studies reported contradictory results regarding abnormalities of mitochondrial transport following mutated MFN2 expression (10, 12, 15). We monitored axonal mitochondrial transport by time-lapse microscopy in vivo, in the mouse sciatic nerve. Mitochondria were classified according to their velocities, moving at either very slow (<0.3 μm/min), slow (>0.3 and <0.6 μm/min), medium (>0.6 and <0.9 μm/min), or fast (>0.9 μm/min) speed (Fig. 6 *A* and *B* and *SI Appendix*, Fig. S3*B*). The frequency distribution showed more very-slow-moving and fewer moving mitochondria in axons of the sciatic nerve of 1-mo-old *CMT2A Tg* mice compared with control mice (*SI Appendix*, Fig. S3*B*). In addition, very-slow-moving mitochondria were significantly slower in *CMT2A Tg* mice, compared with WT littermates (mean speed of very slow mitochondria, WT: 0.24 ± 0.011 μm/min, *CMT2A Tg*: 0.11 ± 0.01 μm/min) (Fig. 6*B*). This actually translated into a sharp increase in the proportion of stationary mitochondria (WT: 3.4%, *CMT2A Tg*: 50.7%). Mitochondrial velocity was not affected toward any specific direction, since there was no difference in the average anterograde or retrograde mitochondrial transport speeds (Fig. 6*C*). However, the proportion of mitochondria moving anterogradely or retrogradely was different between control and *CMT2A Tg* mice (WT: 32% retrograde and 68% anterograde moving mitochondria, *CMT2A Tg*: 55% retrograde and 44% anterograde moving mitochondria). The formation of mitochondria accumulations/clusters has previously been observed in vitro and could potentially be linked to mitochondrial transport defects induced by $MFN2^{R94Q}$ (14, 16). Therefore, we measured the diameter of mitochondria clusters in axons relative to the average diameter of a single mitochondrion. We noticed a significant overrepresentation of individual mitochondria as well as small mitochondria clusters (size category 0.4–0.6 μm) with a decrease in the numbers of large-size clusters in *CMT2A Tg* axons compared with WT axons (Fig. 6*D*). Overall, these observations suggest defects in mitochondrial dynamics following $MFN2^{R94Q}$ overexpression.

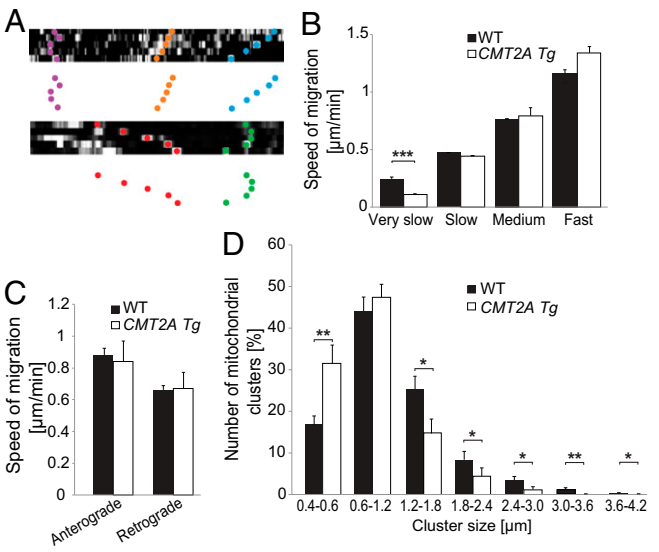

Fig. 6. $MFN2^{R94Q}$ impairs mitochondrial transport and leads to overabundance of small mitochondria clusters in vivo. (*A*) Examples of kymographs used to determine mitochondrial velocity in sciatic nerve axons of 1-mo-old animals. Colored dots represent different types of mitochondrial movements. (*B*) mitochondria are classified according to very slow (<0.3 μm/min), slow (>0.3 and <0.6 μm/min), medium (>0.6 and <0.9 μm/min), and fast (>0.9 μm/min) transport velocities. Statistical analysis: two-tailed unpaired Student's *t* test. (*C*) Mitochondrial anterograde and retrograde transport velocities were evaluated in the sciatic nerve of WT ($n = 74$ mitochondria from seven mice) and *CMT2A Tg* ($n = 29$ mitochondria from six mice) mice. (*D*) Number of mitochondrial clusters according to cluster size in axons of WT ($n = 23$ axons from 10 mice) and *CMT2A Tg* ($n = 16$ axons from six mice) mice. Statistical analysis: two-tailed unpaired Student's *t* test. $*P < 0.05$, $**P < 0.01$, $***P < 0.001$.

$MFN2^{R94Q}$-Induced Changes in Mitochondrial Morphology Can Be Partially Reverted by Preventing ER Stress. MFN2 is one of the main proteins controlling mitochondrial fusion (40). Mitochondrial length is reduced in sensory neurons expressing $MFN2^{R94Q}$ (10). Altered ER–mitochondria contact could be implicated in this phenotype since MAM participate in regulation of mitochondria dynamics (18). We analyzed mitochondria morphology in vitro, by loading motor neurons and sensory neurons with MitoTracker Red, allowing labeling more than 90% of axonal mitochondria (22). We noticed a significant decrease in mitochondria length in both motor and sensory neurons overexpressing $MFN2^{R94Q}$ (motoneurons: $MFN2^{WT}$: 1.76 ± 0.14 μm, $MFN2^{R94Q}$: 1.36 ± 0.09 μm; sensory neurons: $MFN2^{WT}$: 1.79 ± 0.09 μm, $MFN2^{R94Q}$: 1.43 ± 0.09 μm) (Fig. 7 *A* and *B*). Mitochondria morphology was also evaluated using in vivo imaging, in axons of the sciatic nerve of 1-mo-old WT and *CMT2A Tg* mice. In this experiment, axonal mitochondria were labeled with mitoDsred2 expressed following injection of AAV9-CAG-mitoDsred2 into the spinal cord at postnatal day 1. In *CMT2A Tg* mice, mitochondrial length was again significantly reduced compared with WT littermates (WT: 3.7 ± 0.1 μm, *CMT2A Tg*: 3.2 ± 0.12 μm) (Fig. 7 *C* and *D*). The diameter of mitochondria was not significantly changed (WT: 0.49 ± 0.13 μm, *CMT2A Tg*: 0.56 ± 0.1 μm). Furthermore, we also used transmission electron microscopy to assess mitochondrial morphology in the soma of spinal cord motoneurons (*SI Appendix*, Fig. S3*C*). In 12-mo-old *CMT2A Tg* mice, consistent significant decrease in mitochondria length was observed (WT: 0.64 ± 0.014 μm, *CMT2A Tg*: 0.58 ± 0.02 μm). Together, these results suggest that mutated MFN2 may affect mitochondrial fusion, leading to smaller mitochondria.

Since perturbations of ER–mitochondria contacts affect mitochondrial dynamics, we sought to explore if treatments with either Pre-084 to reinforce MAM function or salubrinal to prevent ER stress had beneficial effects on mitochondrial morphology in neurons expressing $MFN2^{R94Q}$. We measured mitochondria length in primary motoneurons expressing $MFN2^{R94Q}$ as previously described and found that both treatments restored mitochondrial length to values similar to the control $MFN2^{WT}$ condition (Fig. 7*E*). By performing electron microscopy on the distal sciatic nerve of 6-mo-old *CMT2A Tg* mice, we also measured a significant rescue of mitochondrial size and density after 4 wk of daily salubrinal injections (Fig. 7 *F*–*H*). Finally, we also evaluated the motor performance of salubrinal-treated *CMT2A Tg* mice compared with saline-injected *CMT2A Tg* and WT animals. In the rotarod test, a significant increase of the latency time until fall was observed only in the salubrinal-treated *CMT2A Tg* mice, compared with the motor performance measured before treatment (Fig. 7*I*). Overall, these results demonstrate that both the modulation of MAM and ER stress support proper function of mitochondria and could prevent some defects caused by $MFN2^{R94Q}$.

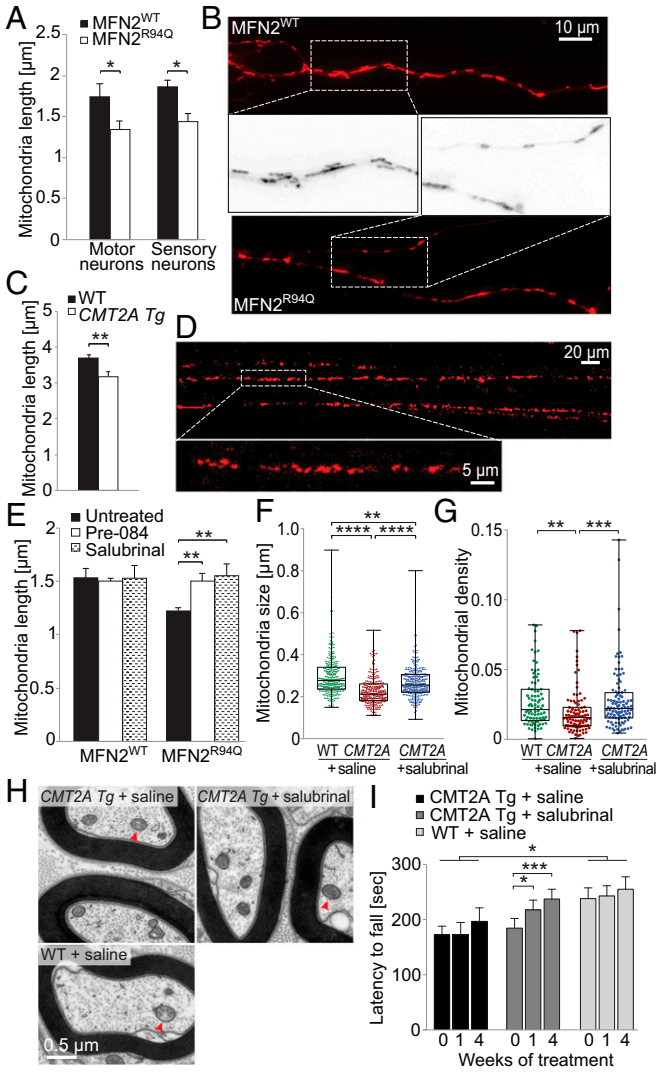

Fig. 7. Mitochondrial morphology is affected by MFN2^{R94Q} both in vitro and in vivo. (*A* and *B*) Motor and sensory neurons infected with AAV6-hsyn-hMFN2^{WT} or AAV6-hsyn-hMFN2^{R94Q} were stained at 6 dpi with MitoTracker Red to assess mitochondria morphology. (*A*) Mitochondrial length quantified in the proximal part of axons (n = 5 independent motoneuron cultures and n = 3 independent sensory neuron cultures). Statistical analysis: two-tailed unpaired Student's t test. (*B*) MitoTracker Red-stained mitochondria in axons of motoneurons expressing either MFN2^{WT} or MFN2^{R94Q}. Higher magnifications of MitoTracker Red-stained mitochondria are shown in the middle. (*C*) Mitochondrial length in sciatic nerve axons of 1-mo-old WT (n = 767 mitochondria from 10 mice) and *CMT2A Tg* (n = 395 mitochondria from six mice) mice. Statistical analysis: two-tailed unpaired Student's t test. (*D*) Representative images of axonal mitochondria stained with AAV9-CAG-mitoDsred2. Images taken with 20× and 63× objectives are from the same area but are time-shifted due to mitochondria movement. (*E*) Mitochondrial length (visualized with MitoTracker Red) quantified at 6 dpi in motoneurons expressing either MFN2^{WT} or MFN2^{R94Q}. Motoneuron cultures were treated with either Pre-084 (50 nM) or salubrinal (5 µM). Results represent n = 3 independent cultures. Statistical analysis: repeated-measure two-way ANOVA with Tukey's post hoc test. (*F*) Box-and-whisker plot of mitochondrial size measured by electron microscopy in distal sciatic nerve axons of 6-mo-old WT (n = 291 mitochondria from three mice), *CMT2A Tg* mice (n = 287 mitochondria from three mice), and *CMT2A Tg* mice daily treated for 4 wk with 1 mg/kg salubrinal (n = 315 mitochondria from three mice). (*G*) Box-and-whisker plot of mitochondrial density measured in the same samples by determining the fraction of axoplasm occupied by mitochondria (WT: n = 86 axons; *CMT2A Tg*: n = 94 axons; *CMT2A Tg* mice + salubrinal: n = 103 axons). Statistical analysis for *F* and *G*: Kruskal–Wallis test with Dunn's multiple comparison post hoc test. (*H*) Representative electron microscopy images of axonal mitochondria (red arrowheads) in distal sciatic nerve axons of 6-mo-old WT and *CMT2A Tg* mice. (*I*) Evaluation of the effect of 4-wk salubrinal treatment on the rotarod performance of 6-mo-old *CMT2A Tg* mice compared with saline-treated animals (*CMT2A Tg* mice + saline, n = 8; *CMT2A Tg* + salubrinal, n = 9 mice; WT + saline, n = 7). Statistical analysis: two-way repeated-measures ANOVA (group × time, significant group and time effects) with Dunnett's (group effect) or Sidak (time effect) post hoc test. *P < 0.05, **P < 0.01, ***P < 0.001, ****P < 0.0001.

Discussion

We used both in vitro and in vivo models of CMT2A diseases to gain insight into the pathophysiology of *MFN2^{R94Q}*-induced axonopathy. Overexpression of *MFN2^{R94Q}* led to partially progressive locomotor impairments in mice, whereas overt distal axonal degeneration was apparent only at later stages of the disease. Decreased numbers of ER–mitochondria contacts as well as ER and mitochondria dysfunction were detected in motor and sensory neurons expressing MFN2^{R94Q}, either preceding or concomitant to axonal degeneration. We also observed that the number of MAM was reduced in patient-derived fibroblasts carrying MFN2 mutations compared with age-matched controls.

Although muscle strength can be affected to different degrees in CMT2A patients depending on the age of disease onset, clinical data also indicate that sensory function is generally less affected (6, 41, 42). Here, we characterized the motor and sensory functions of *CMT2A Tg* mice at early and late stages of the disease (6 vs. 12 mo). We confirmed that locomotor dysfunction is an early feature of *CMT2A Tg* mice, detectable with the rotarod test in 6- and 12-mo-old mice, although this phenotype does not worsen with age. The motor function as evaluated by rotarod is more affected in male than female *CMT2A Tg* mice. To our knowledge, no sex-specific motor deficits have been previously described in CMT patients, except for CMTX1, where males have a tendency (although not reaching statistical significance) to be more affected than females (43).

Locomotion as well as gait defects are most evident in the CatWalk test (44), previously used in another CMT2A model (13). This test has revealed several parameters altered in *CMT2A Tg* mice, which highlight changes in the pressure and the surface of contact of the paw (spatial parameters) and in gait/posture (temporal parameter) and coordination. Spatial parameters are consistently decreased at 6 and 12 mo, whereas temporal parameters and coordination tend to deteriorate over time. Similarly, foot misplacement and deformation, as well as toe muscle weakness, are observed in CMT2A patients and lead to steppage gait (6). In *CMT2A Tg* mice, gait parameters such as terminal dual stance and duty cycle mean are already changed at 6 mo. At 12 mo, parameters including left hindpaw stand mean and support three are significantly changed, which could suggest posture alterations with an increased duration of the postural phase (45). In addition, interpaw coordination of the right limb pair reflected by the phase dispersion and couplings parameters, are altered in 12-mo-old *CMT2A Tg* animals. All together, these results indicate walking difficulties in *CMT2A Tg* mice, with symptoms slightly progressing between 6 and 12 mo.

Quantification of NMJ occupancy showed that between 6 and 12 mo of age the proportion of fully innervated junctions significantly declines to 50% in the slow-twitch soleus muscle of *CMT2A Tg* mice. In contrast, in the fast-twitch tibialis muscle, denervation does not reach statistical significance and electrophysiological recordings do not show any significant changes in CMAP amplitude. Our data show that neuromuscular pathology is more prominent in the slow-twitch soleus muscle compared with the fast-twitch tibialis anterior muscle. It is, however, possible that other distal muscles might be also affected, which will require further analysis. Soleus muscle is mainly involved in walking and maintenance of standing posture (46), two parameters

altered in the *CMT2A Tg* mouse model. In contrast, tibialis muscle is involved in functions such as running and jumping, which require strength. Slowly progressing locomotor deficits combined with late muscle denervation indicate that *CMT2A Tg* mice partially mimic the phenotype of late-onset CMT2A neuropathy. Compared with early-onset disease, late-onset CMT2A is indeed characterized by milder and more slowly progressing symptoms (41). Moreover, axonal degeneration is almost absent in these patients, which is in line with the normal numbers of motoneurons and proximal axons measured in *CMT2A Tg* mice until month 12.

Whereas *CMT2A Tg* mice already display motor impairments at 6 mo, a significant decrease in NMJ occupancy in the soleus muscle is only observed at 12 mo. It was previously shown in another model with pathological changes in the motor system that locomotor deficits can be detected before structural changes at the level of NMJ (47). Of note, MFN2 overexpression can have direct effects on the maintenance of the NMJ, via the axonal transport of calpastatin (48). However, even in a structurally intact NMJ neurotransmission can be affected by cellular mechanisms, such as mitochondrial depletion (49). Furthermore, the dynamic remodeling of the motor units, as shown in a model of amyotrophic lateral sclerosis, may also mask pathological defects at the level of the NMJ for a limited period of time (50).

In agreement with the in vivo data, we observed no decrease in the survival of primary motor and sensory neurons induced to overexpress $MFN2^{R94Q}$ for up to 8 d in vitro. However, we detected substantial neurite shortening and the presence of axonal swellings and spheroids indicating ongoing neurite degeneration. As no motoneuron death is observed, reduction in neuritic length of $MFN2^{R94Q}$ motoneurons may reflect a dying-back process which has already been described in motoneuron diseases (22, 51). Similar to previously published observations, sensory neurons also display signs of axonal degeneration without any reduction in neuritic length (10).

MFN2 regulates ER–mitochondria associations as well as calcium transfer from ER toward mitochondria (17). The connection between these organelles is maintained via interaction of $MFN2^{mitochondrial}$–$MFN2^{ER}$ homodimers or $MFN1^{mitochondrial}$–$MFN2^{ER}$ heterodimers (17, 26, 40). It is still unclear whether MFN2 regulates positively or negatively the formation of MAM (17, 26, 27). Recent work has discriminated the role of short- and long-range ER–mitochondria contacts based on a split green fluorescent protein-based contact site sensor (52). Using this system, it was shown that down-regulation of MFN2 increases short-range ER–mitochondria connections, whereas it reduces the long-range ones, arguing the observed discrepancy regarding the role of MFN2 at MAM. Our data demonstrate that the neuronal overexpression of $MFN2^{R94Q}$ affects ER–mitochondria contacts both in vitro and in vivo. In addition, we observed that the number of MAM is reduced in fibroblasts derived from CMT2A-R94Q patients. Since $MFN2^{R94Q}$ is expressed at a level similar to $MFN2^{WT}$ (8, 17), it is unlikely that the observed defects are due to specific changes in $MFN2^{R94Q}$ abundance at the level of the ER or mitochondria. Alternatively, altered capacity of $MFN2^{R94Q}$ to interact with MFN2 (9) may contribute to the observed decrease in ER–mitochondria contacts. Interestingly, it has been shown that in contrast to MFN2, MFN1 is able to make functional interactions with $MFN2^{R94Q}$ (9). However, since MFN1 localization is restricted to mitochondria, it cannot complement $MFN2^{ER}$ and may therefore only partially rescue the effects of the mutation at the level of ER–mitochondria contacts. Indeed, contrary to its effect on mitochondrial dynamics observed in sensory neurons (10), MFN1 overexpression does not rescue either the number of MAM or neurite shortening in motoneurons overexpressing $MFN2^{R94Q}$.

Disruption of MAM has emerged as a key process in several neurodegenerative diseases (22, 25, 53). MAM regulate various processes essential for neuronal function, such as calcium transfer between ER and mitochondria, which controls ATP production (54). MAM also control lipid synthesis and transfer, as well as mitochondrial dynamics (18). Remarkably, stimulation of the MAM protein SIGMAR1 with the Pre-084 agonist prevented axonal degeneration in motoneurons overexpressing $MFN2^{R94Q}$. SIGMAR1 is an ER chaperone protein involved in the stabilization of IP3R, thereby controlling ER calcium efflux (54). SIGMAR1 inhibition or loss has been connected to MAM defects and axonal degeneration in motoneurons (22, 53).

Disconnection of ER and mitochondria can affect the function of both organelles. Interestingly, previous studies in mice already implicated ER stress in pathophysiology of demyelinating CMTs. Trembler-J (TrJ) mice, which carry a spontaneous L16P point mutation in PMP22 protein and represent a model of CMT1E, show evidence of UPR activation in ER (55). Similarly, mutations in MPZ/P0 which models CMT1B ($P0^{S63del}$) or Dejerine–Sottas syndrome ($P0^{R98C}$) both cause ER stress and activation of UPR (55). We therefore evaluated pathological changes in ER and measured an increase of ER stress markers that occurred in motoneurons both in vitro and in vivo. The potential link between MFN2 and ER stress remains poorly understood. MFN2 depletion in liver and skeletal muscle leads to an increase in P-eIF2α, CHOP, IRE-1, ATF6, and the ER chaperone BIP (56). In cardiac myocytes, the deletion of MFN2, but not MFN1, enhances ER stress (57). UPR aims at reestablishing proper ER function by promoting ER chaperone synthesis and ER-associated protein degradation, as well as decreasing protein translation. However, in case of sustained activation, UPR can lead to cell degeneration (58). MFN2 modulates UPR sensors by direct interaction with PERK (direct activator of P-eIF2α), preventing its constitutive activation (59). Our observation that the ER-stress inhibitor salubrinal prevents axonal degeneration in motoneurons expressing $MFN2^{R94Q}$ suggests that ER stress is likely to contribute to axonal dysfunction in CMT2A.

We have also tried to evaluate the levels of ER stress in CMT2A patient-derived fibroblasts. However, the levels of P-eIF2α and CHOP were highly variable in both control and patients' cells, making it difficult to interpret a possible effect of MFN2 mutation on the basal and induced ER stress. The observed variability may reflect differences between used fibroblast culture that are likely to be linked to their proliferative capacity and/or their number of passages. Alternatively, fibroblasts might also be able to recover more easily from ER stress than neurons in culture conditions.

Disturbances in the regulation of $[Ca^{2+}]_i$ was evident in both sensory and motor neurons overexpressing $MFN2^{R94Q}$ as well as in CMT2A patient-derived fibroblasts compared with their respective controls. Our observation that the discharge of Ca^{2+} from the ER is smaller in CMT2A cells could suggest a disturbance in the refilling of the ER Ca^{2+} pool and/or an increase in ER Ca^{2+} leakage. Store-operated calcium entry dysfunction has been implicated in GDAP1-associated Charcot–Marie–Tooth 4A, where defects in the partial depletion of intracellular Ca^{2+} stores and/or release were reported (60). The increase in capacitative Ca^{2+} entry in CMT2A cells that was unmasked when extracellular Ca^{2+} was removed could reflect a compensatory mechanism aimed at refilling the reduced Ca^{2+} pool in the ER (61). It would be tempting to hypothesize that the impaired ER–mitochondria tethering in CMT2A cells could reduce the direct availability of ATP to power the ER's ATPase activity, resulting in the net loss of Ca^{2+} from the ER into the cytosol. This coupled with the increased capacitative influx of Ca^{2+} may explain the larger CCCP-induced mitochondrial Ca^{2+} responses seen in CMTA2 cells, which could in part reflect a mitochondrial-dependent compensatory mechanism to buffer $[Ca^{2+}]_i$.

Mitochondria can adjust to stress conditions by dividing or fusing. Mitochondrial fusion enables mitochondria to exchange

components and rescue mitochondria, while mitochondrial fission promotes axonal transport and cell apoptosis (62). Mitochondrial fragmentation has been reported in axons of sensory neurons or motoneurons overexpressing $MFN2^{R94Q}$ (10, 14, 16). We indeed observed decreased mitochondria length in vitro, in axons of both motor and sensory neurons overexpressing $MFN2^{R94Q}$, consistent with defects in mitochondrial fusion. Live imaging of mitochondria in intact sciatic nerves of 1-mo-old *CMT2A Tg* mice also showed a reduction in mitochondria length as well as overabundance of small mitochondria clusters. This could indicate that mitochondria tend to be fragmented already in the axons of young *CMT2A Tg* mice. Altered mitochondria dynamics may also underlie some of the behavioral and structural phenotypes seen in older mice, as confirmed by electron microscopy in motoneurons of 12-mo-old *CMT2A Tg* mice.

Defects in mitochondria positioning have been observed in sensory neurons expressing $MFN2^{R94Q}$ (10, 14, 16). However, other reports found mild or no axonal transport defects using in vitro models of CMT2A, such as motoneurons differentiated from CMT2A human iPS cells and sensory neurons expressing $MFN2^{R94W}$ (11, 12, 15). By measuring mitochondrial transport in vivo, we noticed that the velocity of slow-moving mitochondria, which could be defined as oscillation movements, was significantly decreased, which corresponds to an increase in the number of stationary mitochondria in *CMT2A Tg* mice. As oscillatory movements require ATP production (63), the strong reduction observed in *CMT2A Tg* axons may reflect reduced levels of available ATP. Although the levels of ATP have not been measured in the sciatic nerve, OXPHOS complexes and ATP levels are decreased in the brain of 9-mo-old *CMT2A Tg* mice (64). In addition, mitochondria tend to form a higher number of small clusters in the axons of *CMT2A Tg* mice. Accumulations of mitochondria have also been observed in the soma and axons of both sensory and motor neurons in models of CMT2A (8, 13, 14, 16), which may further contribute to mitochondrial transport defects.

It is noteworthy that we observed differences between motor and sensory neurons in the cellular response to $MFN2^{R94Q}$ overexpression. Although changes in calcium homeostasis, number of MAM, and length of mitochondria were observed in both neuronal types, UPR markers and neuritic length remained unchanged in the sensory neurons. This selective vulnerability of motor vs. sensory neurons is consistent with previous reports, which showed selective perturbation of motoneurons induced by defects in the MAM protein SIGMAR1 (22) and ER stress to be specifically induced in motoneuron-based models of amyotrophic lateral sclerosis (65, 66). The finding that motoneurons may be more vulnerable than sensory neurons to defects of the ER–mitochondria system may clarify why the motor function is generally more affected than the sensory function in CMT2A patients (42).

In conclusion, our results show that altered interplay between ER and mitochondria contribute to the axonopathy present in *CMT2A Tg* mice. Therefore, modulation of these mechanisms should be considered as a potential future therapeutic strategy to prevent or delay the onset of CMT2A neuropathy.

Materials and Methods

See *SI Appendix, Supplementary Information Materials and Methods* for a detailed description of materials and methods.

Animals and Behavioral Assessments. In vivo work was performed using the mouse strain B6;D2-Tg (Eno2-MFN2*R94Q) L51Ugfm/J previously described by ref. 8 (alternative name *MitoCharc1*, purchased from The Jackson Laboratories, stock no. 012812). Animals were maintained as heterozygous by crossing $B6;D2\text{-}Tg^{(Eno2\text{-}MFN2*R94Q)/-}$ males with B6;D2F1 females (Janvier). All experiments were done in accordance with Swiss legislation and the European Community Council directive (86/609/EEC) for the care and use of laboratory animals and were approved by the Veterinarian Office of the canton of Vaud and a local ethics committee.

Primary Neuronal Cultures and Fibroblast Cell Lines. Fibroblast cell lines were derived from skin biopsies, obtained from two normal controls and two CMT2A patients (PN198.1 and PN198.3; ref. 67) with a p.Arg94Gln missense mutation in the Mitofusin 2 gene (*MFN2*). Motor and sensory neurons cultures were prepared from E12.5 mouse embryos as previously described (22).

Morphological and Molecular Biology Analysis. The construction and production of AAV viral vectors, PLA assay, Western blotting, immunocytochemistry, immunohistochemistry, calcium imaging, mitochondrial axonal transport, and electron microscopy were performed according to standard methods, details of which are described in *SI Appendix, Supplementary Information Materials and Methods*.

Statistical Analyses and Experimental Design. The applied statistical tests as well as the number of replicates are indicated in the figure legends. For all experiments based on primary cultures, results were obtained from at least three independent cell cultures. $*P < 0.05$, $**P < 0.01$, $***P < 0.001$, and $****P < 0.0001$.

ACKNOWLEDGMENTS. We thank Prof. Peter De Jonghe and Prof. Jonathan Baets, who provided fibroblasts from the CMT2A patients and control individuals; Philippe Colin and Christel Voize for technical support in animal experimentation and histology; Priyanka Ravikumar, Aline Aebi, Fabienne Pidoux, and Viviane Padrun for viral vector production; the electron microscopy platform of École Polytechnique Fédérale de Lausanne, Interdisciplinary Centre for Electron Microscopy, for the processing of the tissues and imaging; Romain Cartoni and Jean-Claude Martinou for their help with *CMT2A tg* mice; and Hassan Boukhaddaoui, the Montpellier Resources Imaging Facility, and the animal facility staff of the SMARTY platform of the Réseau des Animaleries de Montpellier. This work was supported by Swiss National Science Foundation Grant 310030L_156460/1 (to B.L.S.), ERANET E-Rare FaSMALS Grant 3ER30_160673 (to B.L.S.), a Neuromuscular Research Association Basel grant (to B.L.S., R.C., and N.B.-M), a Swedish StratNeuro program grant (to R.C.), Swedish Research Council Grant 2015-02394 (to R.C.), Labex EpiGenMed (G.v.H.), European Research Council Grant FP7-IDEAS-ERC 311610 (to N.T.), AFM-Téléthon Research Grant 20044 (to N.T. and R.C.), Fund for Scientific Research FWO-Flanders Grants G036814N and G041416N (to V.T.), the Queen Elisabeth Medical Foundation (V.T.), the Association Belge contre les maladies neuromusculaires (M.J.), the Sigrid Jusélius Foundation (L.L.), Swedish Brain Foundation Grant FO2018-0209 (to P.U.), and Agence Nationale de la Recherche through the Eranet Neuron III program (C.P.).

1. Azzedine H, Senderek J, Rivolta C, Chrast R (2012) Molecular genetics of Charcot-Marie-Tooth disease: From genes to genomes. *Mol Syndromol* 3:204–214.
2. Weis J, et al. (2017) Towards a functional pathology of hereditary neuropathies. *Acta Neuropathol* 133:493–515.
3. Feely SM, et al. (2011) MFN2 mutations cause severe phenotypes in most patients with CMT2A. *Neurology* 76:1690–1696.
4. Rossor AM, Polke JM, Houlden H, Reilly MM (2013) Clinical implications of genetic advances in Charcot-Marie-Tooth disease. *Nat Rev Neurol* 9:562–571.
5. Züchner S, et al. (2004) Mutations in the mitochondrial GTPase mitofusin 2 cause Charcot-Marie-Tooth neuropathy type 2A. *Nat Genet* 36:449–451, and erratum (2004) 36:660.
6. Stuppia G, et al. (2015) MFN2-related neuropathies: Clinical features, molecular pathogenesis and therapeutic perspectives. *J Neurol Sci* 356:7–18.
7. Chan DC (2006) Dissecting mitochondrial fusion. *Dev Cell* 11:592–594.
8. Cartoni R, et al. (2010) Expression of mitofusin 2(R94Q) in a transgenic mouse leads to Charcot-Marie-Tooth neuropathy type 2A. *Brain* 133:1460–1469.
9. Detmer SA, Chan DC (2007) Functions and dysfunctions of mitochondrial dynamics. *Nat Rev Mol Cell Biol* 8:870–879.
10. Misko AL, Sasaki Y, Tuck E, Milbrandt J, Baloh RH (2012) Mitofusin2 mutations disrupt axonal mitochondrial positioning and promote axon degeneration. *J Neurosci* 32:4145–4155.
11. Rizzo F, et al. (2016) Selective mitochondrial depletion, apoptosis resistance, and increased mitophagy in human Charcot-Marie-Tooth 2A motor neurons. *Hum Mol Genet* 25:4266–4281.
12. Saporta MA, et al. (2015) Axonal Charcot-Marie-Tooth disease patient-derived motor neurons demonstrate disease-specific phenotypes including abnormal electrophysiological properties. *Exp Neurol* 263:190–199.
13. Bannerman P, Burns T, Xu J, Miers L, Pleasure D (2016) Mice hemizygous for a pathogenic mitofusin-2 allele exhibit hind limb/foot gait deficits and phenotypic perturbations in nerve and muscle. *PLoS One* 11:e0167573.
14. Detmer SA, Vande Velde C, Cleveland DW, Chan DC (2008) Hindlimb gait defects due to motor axon loss and reduced distal muscles in a transgenic mouse model of Charcot-Marie-Tooth type 2A. *Hum Mol Genet* 17:367–375.
15. Strickland AV, et al. (2014) Characterization of the mitofusin 2 R94W mutation in a knock-in mouse model. *J Peripher Nerv Syst* 19:152–164.

16. Baloh RH, Schmidt RE, Pestronk A, Milbrandt J (2007) Altered axonal mitochondrial transport in the pathogenesis of Charcot-Marie-Tooth disease from mitofusin 2 mutations. *J Neurosci* 27:422–430.
17. de Brito OM, Scorrano L (2008) Mitofusin 2 tethers endoplasmic reticulum to mitochondria. *Nature* 456:605–610.
18. Krols M, et al. (2016) Mitochondria-associated membranes as hubs for neurodegeneration. *Acta Neuropathol* 131:505–523.
19. Rowland AA, Voeltz GK (2012) Endoplasmic reticulum-mitochondria contacts: Function of the junction. *Nat Rev Mol Cell Biol* 13:607–625.
20. Krols M, et al. (2018) Sensory neuropathy-causing mutations in ATL3 affect ER-mitochondria contact sites and impair axonal mitochondrial distribution. *Hum Mol Genet*, 10.1093/hmg/ddy352.
21. Krols M, et al. (2018) Sensory-neuropathy-causing mutations in ATL3 cause aberrant ER membrane tethering. *Cell Rep* 23:2026–2038.
22. Bernard-Marissal N, Médard JJ, Azzedine H, Chrast R (2015) Dysfunction in endoplasmic reticulum-mitochondria crosstalk underlies SIGMAR1 loss of function mediated motor neuron degeneration. *Brain* 138:875–890.
23. De Vos KJ, et al. (2012) VAPB interacts with the mitochondrial protein PTPIP51 to regulate calcium homeostasis. *Hum Mol Genet* 21:1299–1311.
24. Hedskog L, et al. (2013) Modulation of the endoplasmic reticulum-mitochondria interface in Alzheimer's disease and related models. *Proc Natl Acad Sci USA* 110: 7916–7921.
25. Paillusson S, et al. (2016) There's something wrong with my MAM; the ER-mitochondria axis and neurodegenerative diseases. *Trends Neurosci* 39:146–157.
26. Cosson P, Marchetti A, Ravazzola M, Orci L (2012) Mitofusin-2 independent juxtaposition of endoplasmic reticulum and mitochondria: An ultrastructural study. *PLoS One* 7:e46293.
27. Filadi R, et al. (2015) Mitofusin 2 ablation increases endoplasmic reticulum-mitochondria coupling. *Proc Natl Acad Sci USA* 112:E2174–E2181.
28. Naon D, et al. (2016) Critical reappraisal confirms that mitofusin 2 is an endoplasmic reticulum-mitochondria tether. *Proc Natl Acad Sci USA* 113:11249–11254.
29. Harel T, et al.; Baylor-Hopkins Center for Mendelian Genomics; University of Washington Center for Mendelian Genomics (2016) Recurrent de novo and biallelic variation of ATAD3A, encoding a mitochondrial membrane protein, results in distinct neurological syndromes. *Am J Hum Genet* 99:831–845.
30. Gerber S, et al. (2017) Mutations in DNM1L, as in OPA1, result in dominant optic atrophy despite opposite effects on mitochondrial fusion and fission. *Brain* 140: 2586–2596.
31. Cartoni R, Martinou JC (2009) Role of mitofusin 2 mutations in the physiopathology of Charcot-Marie-Tooth disease type 2A. *Exp Neurol* 218:268–273.
32. Deuis JR, Dvorakova LS, Vetter I (2017) Methods used to evaluate pain behaviors in rodents. *Front Mol Neurosci* 10:284.
33. Lin KL, et al. (2010) DuraSeal as a ligature in the anastomosis of rat sciatic nerve gap injury. *J Surg Res* 161:101–110.
34. Bernard-Marissal N, Sunyach C, Marissal T, Raoul C, Pettmann B (2015) Calreticulin levels determine onset of early muscle denervation by fast motoneurons of ALS model mice. *Neurobiol Dis* 73:130–136.
35. Saxena S, Cabuy E, Caroni P (2009) A role for motoneuron subtype-selective ER stress in disease manifestations of FALS mice. *Nat Neurosci* 12:627–636.
36. Huang P, Yu T, Yoon Y (2007) Mitochondrial clustering induced by overexpression of the mitochondrial fusion protein Mfn2 causes mitochondrial dysfunction and cell death. *Eur J Cell Biol* 86:289–302.
37. Detmer SA, Chan DC (2007) Complementation between mouse Mfn1 and Mfn2 protects mitochondrial fusion defects caused by CMT2A disease mutations. *J Cell Biol* 176: 405–414.
38. Bernard-Marissal N, Chrast R, Schneider BL (2018) Endoplasmic reticulum and mitochondria in diseases of motor and sensory neurons: A broken relationship? *Cell Death Dis* 9:333.
39. Bernard-Marissal N, et al. (2012) Reduced calreticulin levels link endoplasmic reticulum stress and Fas-triggered cell death in motoneurons vulnerable to ALS. *J Neurosci* 32:4901–4912.
40. Chen H, et al. (2003) Mitofusins Mfn1 and Mfn2 coordinately regulate mitochondrial fusion and are essential for embryonic development. *J Cell Biol* 160:189–200.
41. Chung KW, et al. (2006) Early onset severe and late-onset mild Charcot-Marie-Tooth disease with mitofusin 2 (MFN2) mutations. *Brain* 129:2103–2118.
42. Züchner S, Vance JM (2006) Molecular genetics of autosomal-dominant axonal Charcot-Marie-Tooth disease. *Neuromolecular Med* 8:63–74.
43. Cornett KM, et al.; Inherited Neuropathies Consortium (2016) Phenotypic variability of childhood Charcot-Marie-Tooth disease. *JAMA Neurol* 73:645–651.
44. Hamers FP, Koopmans GC, Joosten EA (2006) CatWalk-assisted gait analysis in the assessment of spinal cord injury. *J Neurotrauma* 23:537–548.
45. Wang XH, et al. (2012) Quantitative assessment of gait and neurochemical correlation in a classical murine model of Parkinson's disease. *BMC Neurosci* 13:142.
46. Kanning KC, Kaplan A, Henderson CE (2010) Motor neuron diversity in development and disease. *Annu Rev Neurosci* 33:409–440.
47. Yin Z, et al. (2017) Progressive motor deficit is mediated by the denervation of neuromuscular junctions and axonal degeneration in transgenic mice expressing mutant (P301S) tau protein. *J Alzheimers Dis* 60(Suppl 1):S41–S57.
48. Wang L, et al. (2018) Mitofusin 2 regulates axonal transport of calpastatin to prevent neuromuscular synaptic elimination in skeletal muscles. *Cell Metab* 28:400–414.e8.
49. Guo X, et al. (2005) The GTPase dMiro is required for axonal transport of mitochondria to Drosophila synapses. *Neuron* 47:379–393.
50. Martineau É, Di Polo A, Vande Velde C, Robitaille R (2018) Dynamic neuromuscular remodeling precedes motor-unit loss in a mouse model of ALS. *eLife* 7:e41973.
51. Selvaraj BT, Frank N, Bender FL, Asan E, Sendtner M (2012) Local axonal function of STAT3 rescues axon degeneration in the pmn model of motoneuron disease. *J Cell Biol* 199:437–451.
52. Cieri D, et al. (2018) SPLICS: A split green fluorescent protein-based contact site sensor for narrow and wide heterotypic organelle juxtaposition. *Cell Death Differ* 25: 1131–1145.
53. Watanabe S, et al. (2016) Mitochondria-associated membrane collapse is a common pathomechanism in SIGMAR1- and SOD1-linked ALS. *EMBO Mol Med* 8:1421–1437.
54. Hayashi T, Rizzuto R, Hajnoczky G, Su TP (2009) MAM: More than just a housekeeper. *Trends Cell Biol* 19:81–88.
55. Volpi VG, Touvier T, D'Antonio M (2017) Endoplasmic reticulum protein quality control failure in myelin disorders. *Front Mol Neurosci* 9:162.
56. Sebastián D, et al. (2012) Mitofusin 2 (Mfn2) links mitochondrial and endoplasmic reticulum function with insulin signaling and is essential for normal glucose homeostasis. *Proc Natl Acad Sci USA* 109:5523–5528.
57. Ngoh GA, Papanicolaou KN, Walsh K (2012) Loss of mitofusin 2 promotes endoplasmic reticulum stress. *J Biol Chem* 287:20321–20332.
58. Xiang C, Wang Y, Zhang H, Han F (2017) The role of endoplasmic reticulum stress in neurodegenerative disease. *Apoptosis* 22:1–26.
59. Muñoz JP, et al. (2013) Mfn2 modulates the UPR and mitochondrial function via repression of PERK. *EMBO J* 32:2348–2361.
60. Barneo-Muñoz M, et al. (2015) Lack of GDAP1 induces neuronal calcium and mitochondrial defects in a knockout mouse model of Charcot-Marie-Tooth neuropathy. *PLoS Genet* 11:e1005115.
61. Secondo A, Bagetta G, Amantea D (2018) On the role of store-operated calcium entry in acute and chronic neurodegenerative diseases. *Front Mol Neurosci* 11:87.
62. Milone M, Benarroch EE (2012) Mitochondrial dynamics: General concepts and clinical implications. *Neurology* 78:1612–1619.
63. Gonzalez S, et al. (2015) In vivo time-lapse imaging of mitochondria in healthy and diseased peripheral myelin sheath. *Mitochondrion* 23:32–41.
64. Guillet V, et al. (2011) Bioenergetic defect associated with mKATP channel opening in a mouse model carrying a mitofusin 2 mutation. *FASEB J* 25:1618–1627.
65. Langou K, et al. (2010) AAV-mediated expression of wild-type and ALS-linked mutant VAPB selectively triggers death of motoneurons through a Ca2+-dependent ER-associated pathway. *J Neurochem* 114:795–809.
66. Taiana M, Sassone J, Lauria G (2016) Mutant SOD1 accumulation in sensory neurons does not associate with endoplasmic reticulum stress features: Implications for differential vulnerability of sensory and motor neurons to SOD1 toxicity. *Neurosci Lett* 627:107–114.
67. Verhoeven K, et al. (2006) MFN2 mutation distribution and genotype/phenotype correlation in Charcot-Marie-Tooth type 2. *Brain* 129:2093–2102.